Aluminum (Oxy)nitride thin films grown by fs-PLD as electron emitters for thermionic applications

Cite as: AIP Conference Proceedings **2416**, 020004 (2021); https://doi.org/10.1063/5.0068496
Published Online: 05 November 2021

Alessandro Bellucci, Stefano Orlando, Marco Girolami, et al.

Aluminum (Oxy)nitride Thin Films Grown by fs-PLD as Electron Emitters for Thermionic Applications

Alessandro Bellucci[1, a)], Stefano Orlando[2], Marco Girolami[1], Matteo Mastellone[1,3], Valerio Serpente[1], Barbara Paci[4], Amanda Generosi[4], Alessio Mezzi[5], Saulius Kaciulis[5], Riccardo Polini[1,6] and Daniele M. Trucchi[1]

[1]*ISM-CNR, Istituto di Struttura della Materia, DiaTHEMA Lab, Via Salaria km 29.300, 00015 Monterotondo (RM), Italy.*

[2]*ISM-CNR, Istituto di Struttura della Materia, FemtoLab, Contrada Santa Loja, 85050 Tito Scalo - Zona Industriale (PZ), Italy.*

[3]*Dipartimento di Scienze di Base e Applicate per l'Ingegneria (SBAI), Università La Sapienza, Via Antonio Scarpa, 14 - 00161 Roma, Italy.*

[4]*ISM-CNR, Istituto di Struttura della Materia, Femto Lab, Via del Fosso del Cavaliere, 100, 00133Roma, Italy.*

[5]*ISMN-CNR, Istituto per lo Studio dei Materiali Nanostrutturati, Via Salaria km 29.300, 00015 Monterotondo (RM), Italy.*

[6] *Dipartimento di Scienze e Tecnologie Chimiche, Università di Roma "Tor Vergata", Via della Ricerca Scientifica, 1 - 00133 Roma, Italy.*

[a)]Corresponding author: alessandro.bellucci@cnr.it

Abstract. Thin films based on aluminum nitride were obtained by fs-laser assisted Pulsed Laser Deposition (fs-PLD) at room temperature on tantalum substrates for studying the electron emission performance in the temperature range 700-1600 °C, so to investigate the possibility of their exploitation as thermionic cathodes. Results of structural, chemical and morphological analyses show the growth of nanostructured thin films with a significant oxygen contamination, forming a mixture of crystalline aluminum nitride and aluminum oxide as well as metallic aluminum inclusions. Despite the considerable presence of oxygen, the developed cathodes demonstrate to possess promising thermionic emission characteristics, with a work function of 3.15 eV, a valuable Richardson constant of 20.25 A $cm^{-2}K^{-2}$, and a highly thermo-electronic stability up to operating temperatures of 1600 °C.

INTRODUCTION

In the last decade, solid-state converters for concentrated solar power are attracting a progressively growing interest thanks to their reliability, low maintenance cost and scalability if compared to conventional thermodynamic heat engines. The main solid-state technology is given by concentrated photovoltaic cells (CPVs), which are considered the most profitable systems for exploiting the concentrated solar radiation. Outstanding conversion efficiencies at lab-scale up to 47.1% have been recently obtained with a 6-junction CPVs [1]. However, multi-junction CPVs suffer generally from serious performance reduction with increasing operating temperature and, consequently, they imply the necessity to be efficiently cooled. Alternatively, the concepts of thermophotovoltaic cells (TPVs) and thermionic solid-state converters (TECs) are based on the use of a solar absorber, which acts as thermal emitter of photons for

NanoInnovation 2020
AIP Conf. Proc. 2416, 020004-1–020004-9; https://doi.org/10.1063/5.0068496
Published by AIP Publishing. 978-0-7354-4133-0/$30.00

TPVs [2] and as electron emitter for TECs [3]. TECs exploit the electron emission at high temperature from a cathode formed by low work function materials [4], and the collection of the generated electrical current by the anode, operating at lower temperature and matched to the cathode work function for the generation of an output voltage. Moreover, hybrid solutions involving TECs have recently been considered very promising conversion systems for advantageous electrical power production [5]. Among them, two proposed systems result significantly promising: 1) the concept of solar thermionic-thermoelectric generator (ST^2G) [6], which provides a theoretical conversion efficiency, calculated under realistic conditions, of 41.1% at 100 W/cm^2 of input power density; 2) the use of photovoltaic anodes in thermionic converters (namely, TIPV), that has been recently demonstrated to enhance the thermionic performances [7], leading the path to hybrid TIPV devices with enhanced electrical output power density with respect to the two independent converters [8, 9] to be used as topping cycle converters or even to exploit novel thermal storage systems operating at ultra-high temperatures [10]. When photons and thermal energy act in combination, the photon-enhanced thermionic emission (PETE) mechanism [11] can be exploited to obtain lower operating temperature and higher conversion efficiency thermionic converters than pure TECs. Bandgap-engineering [12] and defect-engineering [13, 14] strategies were proposed and developed for the fabrication of efficient PETE cathodes, although this technology is still not mature to be presently competitive [15].

For all the above-mentioned cases, the thermionic-based converter structure needs a work function (ϕ) engineering for the two involved electrodes: the cathode work function must be as low as possible but higher than that of the anode to maximize the output voltage. Not only: the cathode should be both a good electrical and thermal conductor and resistant at the operating temperatures. This technological feature is one of the main requirements for achieving significant performances of thermionic-based converters, together with the necessity of maintaining inter-electrode spacing of few μm through engineered dielectric microspacers [16].

The most used approach for ϕ-reduction is the deposition of engineered coatings on proper substrates. Indeed, the use of alkali-metal coatings (Cs, Ba, CsO, BaO, etc.) is known to allow a reduction of the work function for many materials, but this solution suffers from low thermal stability at high operating temperatures and it is usually considered for the surface anode technology [17]. Alternatively, thin-films of hydrogen-terminated diamond [18] and lanthanum (oxy)hexaboride [19, 20] on refractory metals, such as tantalum (Ta), tungsten (W) or molybdenum (Mo), showed promising low values of work function in the temperature range up to 700 °C and 1350 °C, respectively, but both the structures exhibited a low Richardson constant that affected the overall thermionic performance.

Here the thermionic performance of aluminum nitride (AlN)-based coatings deposited by fs-PLD on Ta substrates is reported. AlN is a wide bandgap (6.1 eV) semiconductor with excellent thermal and electronic properties typical of wide bandgap semiconductors, such as high thermal conductivity, high chemical resistance, and high melting point [21]. Moreover, it has also been reported that it presents negative electron affinity [22]. Thus, this material is a potential candidate for many technological applications, such as thermionic energy conversion. The properties of field electron emission have been already investigated [23, 24], but to the best of our knowledge, no published report deals with thermionic measurements from AlN thin films. Moreover, even if AlN thin films were already deposited by PLD assisted by ns-laser [25], this work represents the first production by fs-PLD.

FABRICATION AND CHARACTERIZATION OF THERMIONIC CATHODES

The proposed thermionic cathodes were fabricated by depositing a thin film with thickness of 100 nm on polycrystalline Ta cylindrical substrates (10 mm diameter, 8 mm height), according to an optimized recipe which maximized the thermally-stimulated electron emission capabilities.

The experimental setup for deposition is a PLD system equipped with a Spectra Physics Spitfire Pro XP Ti:Sapphire ultra-short pulsed laser source (800 nm wavelength, pulse duration of ~100 fs; repetition rate of 200 Hz; energy of 3.7 ± 0.1 mJ/pulse). The laser beam was directed through a quartz transparent window towards a stainless-steel vacuum chamber, evacuated by a turbo-molecular pump down to a base pressure of 8×10^{-7} mbar. The AlN target (1-inch diameter target produced by Mateck GmbH, 99.9% purity), on which the laser beam was focused at an angle of 45 degrees by a 1.0 m focal lens, was placed on a rotating holder during ablation to avoid cratering. The Ta substrates were ultrasonically cleaned in n-hexane and then positioned on a sample holder maintained at ~ 35 mm from the target.

In order to investigate the structural properties and the crystallinity of the deposited thin films, Raman spectroscopy and X-ray diffraction (XRD) experiments spectra were performed.

Raman spectra were obtained by a Renishaw In-Via spectrometer, equipped with a 457 nm laser in standard confocal mode. The measurements were optimized combining 2400 cm/line grid with a 100× optical enlargement, setting the laser power at 5% of its maximum intensity and acquiring 50 accumulations for t = 10 s/point.

allowed evaluating the films crystalline structure. XRD analysis was performed by means of a Panalytical Empyrean Diffractometer, working in reflection mode and using Cu Kα radiation (λ=1.5418 Å). In the adopted Bragg-Brentano configuration the incident optical pathway uses divergent slits and detection is performed by means of a hybrid Pix'cel 3D solid-state detector, working in 1D linear mode. Samples were studied according to the diffraction angle range $10° < 2\theta < 110°$.

Chemical properties were investigated by X-ray photoelectron spectroscopy (XPS) and ultraviolet photoelectron spectroscopy (UPS), carried out by using a ESCALAB 250 Xi (Thermo Fisher Scientific, UK) spectrometer, equipped with a monochromatized Al Kα (1486.7 eV) and ultraviolet He I (21.2 eV) and He II (40.8 eV) sources, and a 6-channeltron detection system. XPS measurements were carried out at 90-degree take-off angle and standard electromagnetic lens mode, resulting in 1 mm diameter of analyzed sample area. The work function ϕ of the samples was derived by measuring the characteristic cut-off energy in the He I spectra with the application of a negative voltage bias to shift the spectra from the spectrometer threshold [26].

The surface morphology was investigated by field emission scanning electron microscopy (FE-SEM, LEO Supra 35), equipped with an energy dispersive X-ray spectroscopy module (EDS, Oxford Instruments mod. INCA 300).

Thermionic electron emission measurements were performed in an ultra-high vacuum chamber (base pressure of 5×10^{-8} mbar). The cathodes were heated up to 1600 °C by a continuous-wave laser diode (808 nm wavelength) and their temperature was externally measured through a ZnSe viewport with an optical pyrometer focused on one side of the sample. Electrons emitted from the cathode surface were collected by a cooled anode at a distance of 100 μm. The anode was biased for performing current-voltage measurements with a Keithley 617, used both as voltage source and ammeter, in order to evaluate thermionic emission without space-charge conditions.

RESULTS

In this section, we report first the main structural, chemical and morphological characteristics of the optimized AlN-based thin films obtained with fs-PLD and, after that, the results of the thermionic emission measurements will be shown and discussed.

As results from micro-Raman spectroscopy, the five main vibration modes of aluminum nitride A_1 (transverse optical, TO), E_2, E_1 (TO), A_1 (longitudinal optical, LO) and E_1 (LO) were observed, as reported in Fig. 1. The characteristic peaks were found at 479, 587, 634, 786 and 825 cm^{-1}, respectively, resulting to be strongly shifted towards lower wavenumbers, if compared to the case of bulk or micro-structured AlN [27, 28]. The positions were calculated using the Lorentzian function fitting (inset of Fig. 1). In Raman spectra, the peak shifting is related to bond lengths and, indirectly, to a structural stress/strain: shifts to lower wavenumbers are representative of longer bond lengths, thus suggesting a structural strain of the deposited films.

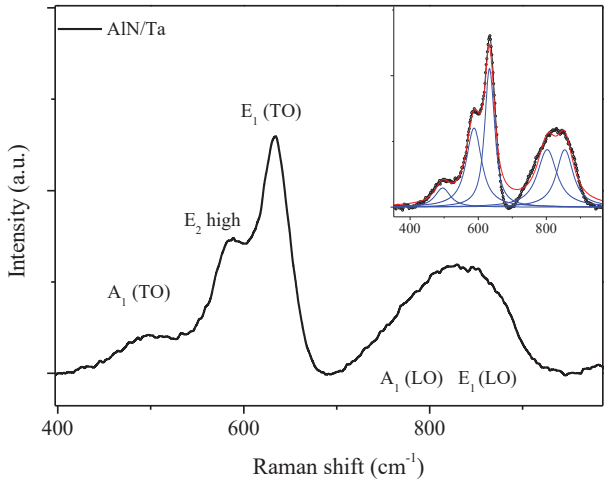

FIGURE 1. Micro Raman spectra of typical AlN films on tantalum substrates. In the inset, the fitting results by Lorentzian curves, to obtain the deconvolution of the five characteristic AlN modes.

The XRD analyses outline the presence of hexagonal AlN (corresponding to Reference code: 96-901-1658). The most intense reflections were detected and labelled in Fig. 2. Additionally, hints of heaxagonal aluminum oxide (Al_2O_3) formation were found (Reference code: 96-900-7635), indicating that crystalline islands of oxides are also present. Grain size was estimated by means of Sherrer's equations and resulted to be in the 25-35 nm range for AlN and ranging from 20 to 40 nm for Al_2O_3.

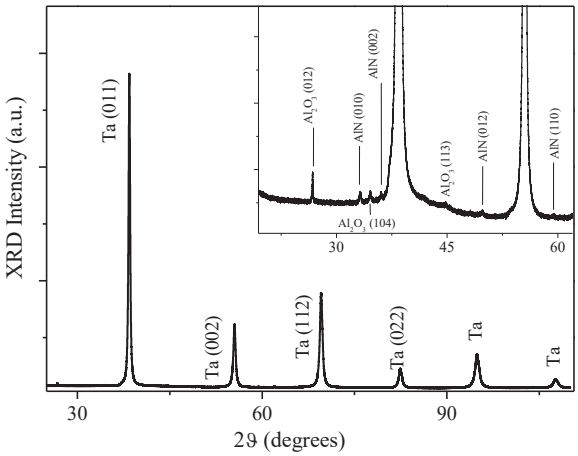

FIGURE 2. XRD spectrum of a typical sample deposited with fs-PLD at room temperature. In the inset, the main reflections of AlN and Al_2O_3 are highlighted. Other minor contributions were also detected.

XPS depth profile (Fig. 3) indicates a bulk (i.e., below the first 10 nm) Al/N atomic concentration ratio of 3, which is far from the correct stoichiometry (ratio of 1). The excess Al atoms reasonably form Al_2O_3 crystalline oxides, that were also detected by XRD, and presumably amorphous oxide phases. The presence of oxygen is indeed clearly highlighted in Figure 3: beyond the surface oxidation, where oxygen tends to form N-O and Al-O compounds (as well as C-O species not reported here, due to a non-negligible amount of carbon in the topmost layers of the films), a significant atomic concentration of oxygen is found through the thickness of the films.

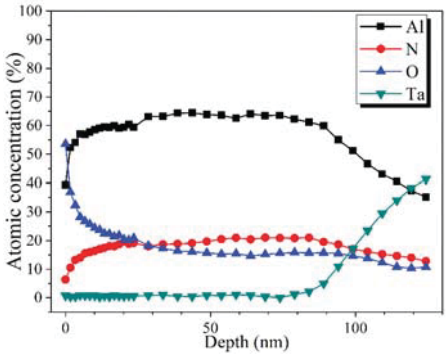

FIGURE 3. XPS depth profile for Al, N, O and Ta elements (C 1s peak was not considered since disappeared after 30 s of cleaning by Ar^+ sputtering).

The peak-fitting analysis of Al 2p, N 1s and O 1s peaks (Fig. 4) allows comprehending the chemical composition of the thin films. In fact, the investigation of the Al 2p peak shows the presence of three components, positioned at different binding energies (BE) for Al $2p_{3/2}$: Al-Al at BE = 71.8 eV, Al-N at BE = 73.8 eV, and Al-O at BE = 74.5 eV. By quantifying the different atomic contributions, only 34.9% of Al atoms is exclusively bonded to nitrogen, whereas the content of metallic Al is 21.2%, with the remaining amount (43.9%) forming oxides. At the same time, the deconvolution of the N 1s and O 1s peak does not exclude the formation of N-O bonds, since the sub-peaks located at BE = 398.3 eV and BE = 532.4 eV for N 1s and O 1s, respectively, are assigned to the N-O surface species [29].

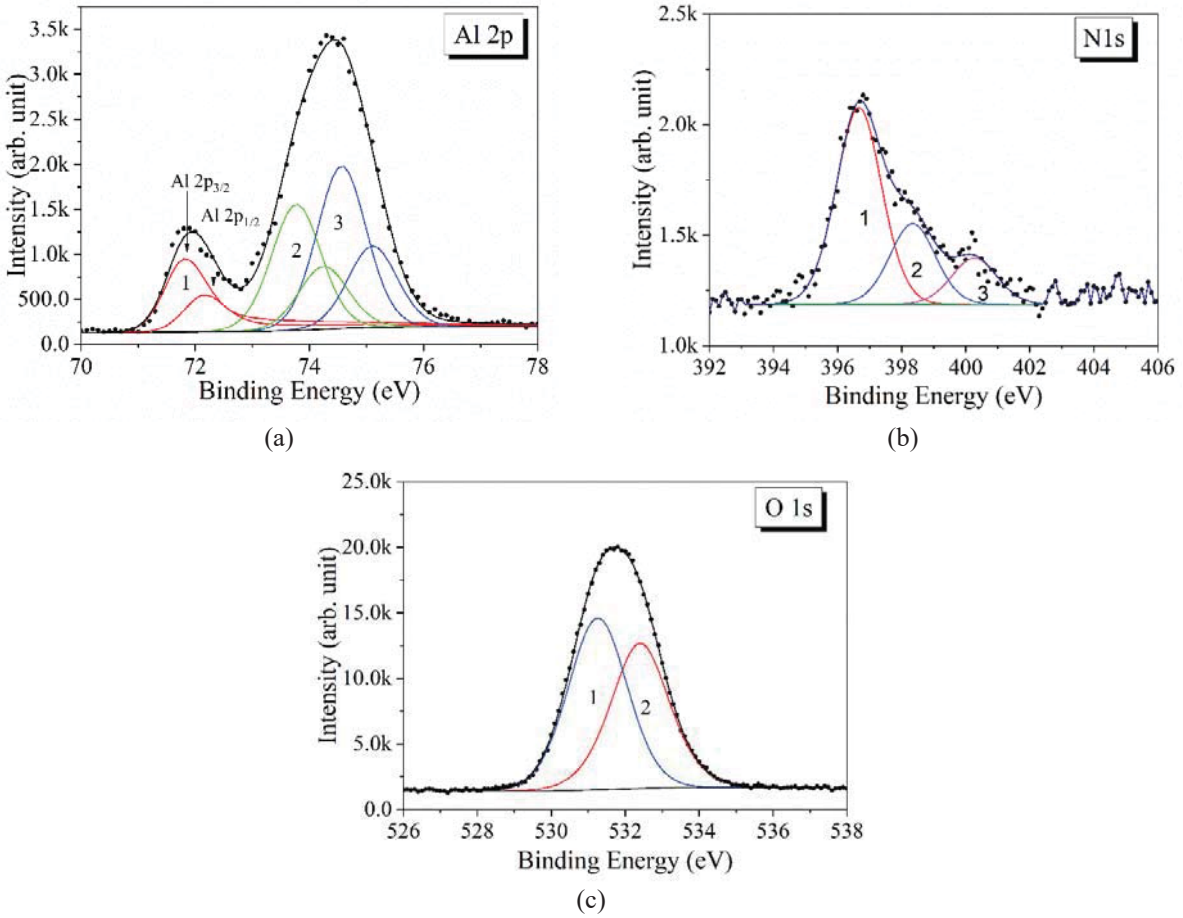

FIGURE 4. XPS peak fitting of: (a) Al 2p, (b) N 1s, and (c) O 1s spectra.

Correlating the XRD and XPS results, it is possible to notice that the Al atomic concentration is even larger than the amount necessary for the deemed formation of both crystalline AlN and Al_2O_3, even if all the nitrogen and oxygen atoms form these compounds. However, even if undesired, the presence of excess metallic Al can be beneficial for the electron emission, since it can be useful for providing conductive paths from the film volume to the surface, which allow electron refilling towards the emitting surface. SEM picture is shown in Fig. 5. The nanostructured nature of the thin films deposited by fs-laser PLD could facilitate the formation of metallic grain-boundaries surrounding nanocrystals of AlN and Al_2O_3 that form the film matrix. It is important to notice the presence of a high amount of micrometer-size aggregates of material (i.e., droplets) over the nanometer-sized film grains, that represent a disadvantage for the thermionic emission since they are positioned on the emitting surface.

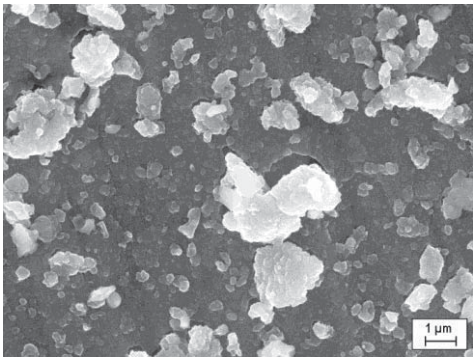

FIGURE 5. SEM image of AlN-based thin films on Ta substrates (50kX magnification).

UPS was used to estimate the work function ϕ, which is the most important property for a material to be used as emitter in thermionic applications, and is a characteristic depending mainly on the material surface. The valence band spectrum used for ϕ calculation is shown in Fig. 6. For these films, the work function estimation was 2.8 ± 0.1 eV, which is significantly lower than the values reported for intrinsic semiconducting AlN [30], all ranging between 3.90 and 5.35 eV. Most probably, this can be explained by the presence of metallic grain-boundaries in our deposited AlN films (not present in pure AlN), which could act as electronic defects inducing a shift of the Fermi level, and consequently a lower value of ϕ. It is also worth mentioning here that the value of 2.8 eV was found before and after the Ar^+ sputtering performed to remove carbon-based (C-C and C-O) surface contaminants (1-2 topmost monolayers): therefore, detrimental effects of the topmost oxides formed when the sample is exposed to the atmosphere can be excluded.

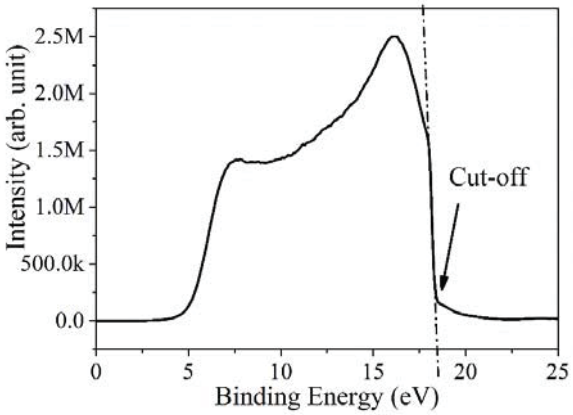

FIGURE 6. Valence band spectrum acquired by applying - 10 V bias voltage. The cut-off indicates the value of the work function as the difference between the energy of the He I line (21.2 eV) and the energy value obtained with the intercept of the cut-off line (18.4 eV).

Finally, thermionic measurements (whose experimental setup is shown in Fig. 7a) were performed in the temperature range between 700 and 1600 °C. The thermionic current density was measured by applying an electric

field between the cathode and the electron collector able to avoid space-charge effects. The saturation current density J_{TI} was evaluated according to the method described elsewhere [31], in order to have an accurate estimation beyond the applied voltages. The temperature dependence of J_{TI} is shown in Fig. 7b. Richardson plot (Fig. 7c) was used for evaluating the ϕ value and the Richardson constant (A_R) with the best accuracy. The derived values of 3.15 ± 0.09 eV and 20.25 ± 2.11 A/cm^{2}K^2 for ϕ and A_R, respectively, make AlN-based thin films deposited by fs-PLD competitive for thermionic emitters operating over 1500 °C, also considering the high stability of the saturation current density verified under long-time continuous operations (Fig. 7d). The difference between UPS and thermionic measurements, ranging between 0.16 and 0.44 eV once considered the measurement errors, could be ascribable to variations with temperature in the activation/deactivation of surface electronic states involved in the electron emission.

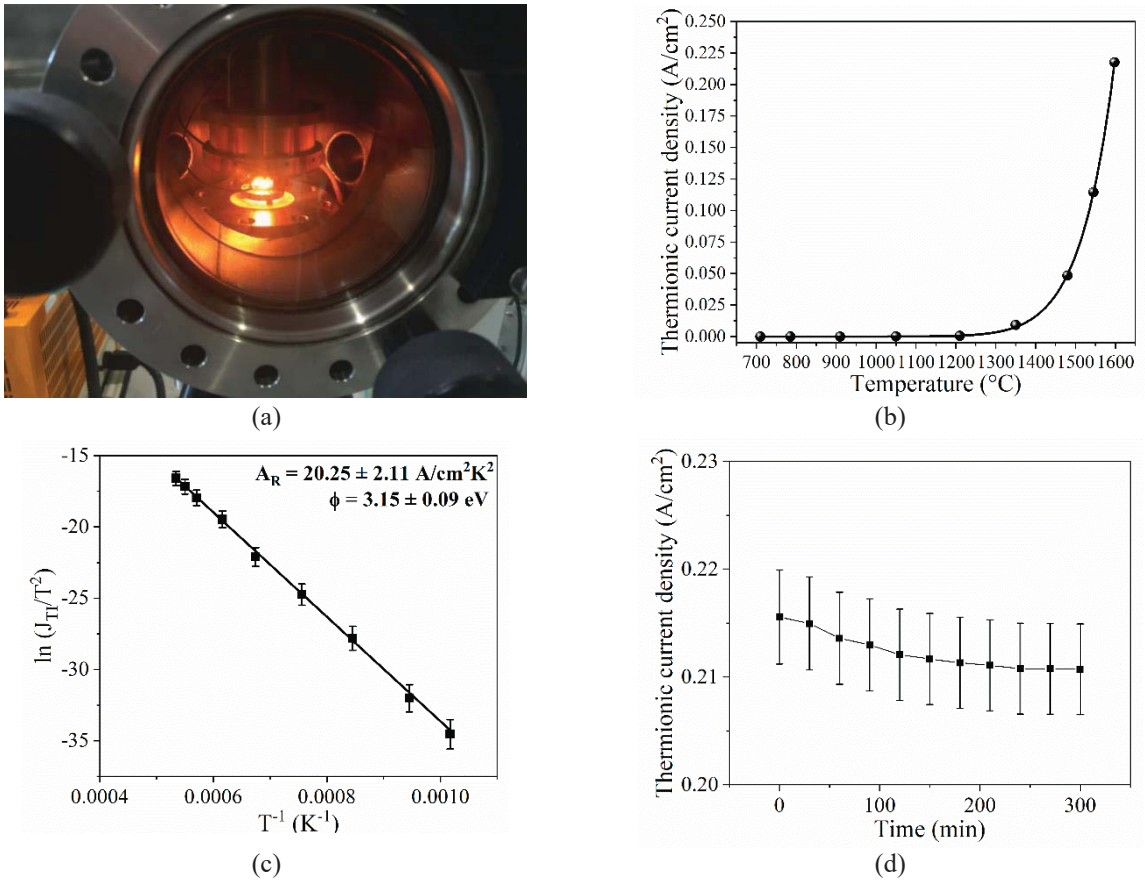

FIGURE 7. (a) Picture of the experimental setup for thermionic measurements with the thermionic cathode at a temperature of 1600 °C; (b) thermionic current density as a function of the cathode temperature T; (c) Richardson plot for the evaluation of the work function and Richardson constant according to the equation $\ln(J_{TI}/T^2) = \ln(A_R) - \phi/(k_B T)$, where k_B is the Boltzmann constant; (d) Monitoring of J_{TI} at the maximum operating temperature (1600 ± 18 °C) as a function of time.

CONCLUSIONS

Nanocrystalline thin films of aluminum (oxy)nitride were grown on tantalum substrates by using fs-PLD for the first time. The presence of oxygen through the thickness of the thin films induced the formation of crystalline Al_2O_3 traces in combination with nanostructured AlN. Aluminum in metallic state, detected by XPS, is probably present locally on the grain boundaries, giving rise to percolative paths useful for the electron conduction and consequent emission, as highlighted by a work function value lower than that of pure intrinsic AlN. UPS measurements resulted

in an estimation of the work function of 2.8 eV, whereas thermionic measurements in the range 700 – 1600 °C, allowing for an absolute evaluation of ϕ, returned more realistically to 3.15 eV. Anyway, the work function value is sufficiently low for emitters operating at $T > 1500$ °C, especially considering the significantly high Richardson constant of 20.25 A/cm^{2}K^2. A saturation current density of 0.225 A/cm^2 at 1600 °C was measured to be sufficiently stable as a function of time after several hours of operation.

ACKNOWLEDGMENTS

This work has been funded by project AMADEUS, which has received funds from the European Union Horizon 2020 research and innovation program, FET-OPEN action, under Grant Agreement 737054. The sole responsibility for the content of this publication lies with the authors. It does not necessarily reflect the opinion of the European Union. Neither the REA nor the European Commission are responsible for any use that may be made of the information contained therein. The authors are grateful to Marco Guaragno (CNR-ISM) for his technical support with X-ray experiments.

REFERENCES

[1] J. F. Geisz, R. M. France, K. L. Schulte, M. A. Steiner, A. G. Norman, H. L. Guthrey, M. R. Young, T. Song and T. Moriarty, Nat. Energy **5**, 326–335 (2020).
[2] T. Bauer, Thermophotovoltaics (Springer, Berlin, Heidelberg, 2011).
[3] G. N. Hatsopoulos and E. P. Gyftopoulos, Thermionic Energy Conversion, Vol. 1: Processes and Devices (The MIT Press, Cambridge, 1973).
[4] D. M. Trucchi and N.A. Melosh, MRS Bulletin **42**, 488-492 (2017).
[5] A. Bellucci, P. Calvani, E. Cappelli, S. Orlando, D. Sciti, R. Yogev, A. Kribus, and D.M. Trucchi, AIP Conf. Proc. **1667**, 020007(2015).
[6] D. M. Trucchi, A. Bellucci, M. Girolami, P. Calvani, E. Cappelli, S. Orlando, R. Polini, L. Silvestroni, D. Sciti, and A. Kribus, Adv. Energy Mater. **8**, 1802310 (2018).
[7] A. Bellucci, M. Mastellone, V. Serpente, M. Girolami, S. Kaciulis, A. Mezzi, D. M. Trucchi, E. Antolín, J. Villa, P. G. Linares, A. Martí, and A. Datas, ACS Energy Lett. **5**, 1364−1370 (2020).
[8] A. Datas, Appl. Phys. Lett., **108**, 143503 (2016).
[9] A. Datas, R. Vaillon, Nano Energy **61**, 10−17 (2019).
[10] A. Datas, A. Belén-Cristobal, C. del Cañizo, E. Antolín, M. Beaughon, N. Nikolopoulos, A. Nikolopoulos, M. Zeneli, N. Sobczak, W. Polkowski, M. Tangstad, J. Safarian, D. M. Trucchi, A. Bellucci, M. Girolami, R. Marx, D. Bestenlehner, S. Lang, A. Vitulano, G. Sabbatella, and A. Martí, AIP Conference Proceedings **2033**, 170004 (2018).
[11] J. Schwede, I. Bargatin, D.C. Riley, B.E. Hardin, S.J. Rosenthal, Y. Sun, F. Schmitt, P. Pianetta, R. T. Howe, Z.-X. Shen and N. A. Melosh, Nat. Mater. **9**, 762 (2010).
[12] J. W. Schwede, T. Sarmiento, V. K. Narasimhan, S. J. Rosenthal, D. C. Riley, F. Schmitt, I. Bargatin, K. Sahasrabuddhe, R. T. Howe, J. S. Harris, N. A. Melosh and Z.-X. Shen, Nat. Commun. **4**, 1576 (2013).
[13] P. Calvani, A. Bellucci, M. Girolami, S. Orlando, V. Valentini, R. Polini and D. M. Trucchi, Carbon **105**, 401-407 (2016).
[14] M. Girolami, L. Criante, F. Di Fonzo, S. Lo Turco, A. Mezzetti, A. Notargiacomo, M. Pea, A. Bellucci, P. Calvani, V. Valentini, D. M. Trucchi, Carbon **111**, 48-53 (2017).
[15] A. Bellucci, M. Girolami, M. Mastellone, S. Orlando, R. Polini, A. Santagata, V. Serpente, V. Valentini, D.M. Trucchi, Nanotechnology **32**, 024002 (2021).
[16] A. Bellucci, G. Sabbatella, M. Girolami, M. Mastellone, V. Serpente, A. Mezzi, S. Kaciulis, B. Paci, A. Generosi, R. Polini, A. Vitulano, I. Vivaldi, M. Antonelli, and D. M. Trucchi, Energy Technol. **9**, 2000788 (2021).
[17] V. Serpente, A. Bellucci, M. Girolami, M. Mastellone, A. Mezzi, S. Kaciulis, R. Carducci, R. Polini, V. Valentini, and D.M. Trucchi, Materials Chemistry and Physics **249**,122989(2020).
[18] F. A. M. Koeck, R. J. Nemanich, J. Appl. Phys. **112**, 113707 (2012).

[19] A. Bellucci, M. Mastellone, S. Orlando, M. Girolami, A. Generosi, B. Paci, P. Soltani, A. Mezzi, S. Kaciulis, R. Polini, and D. M. Trucchi, App. Surf. Sci. **479**, 269-302 (2019).
[20] A. Bellucci, M. Mastellone, M. Girolami, V. Serpente, A. Generosi, B. Paci, A. Mezzi, S. Kaciulis, R. Carducci, R. Polini, S. Orlando, A. Santagata, A. De Bonis, M. Meucci, L. Mercatelli, E. Sani, D.M. Trucchi, App. Surf. Sci. **513**, 145829 (2020).
[21] S. Strite and H. Morkoc¸, J. Vac. Sci. Technol. B **10**, 1237 (1992).
[22] R. J. Nemanich, P. K. Baumann, M. C. Benjamin, S. W. King, J. van der Weide, R. F. Davis, Diam. Relat. Mater. **5**, 790-796 (1996).
[23] V. N. Tondare, C. Balasubramanian, S. V. Shende, D. S. Joag, V. P. Godbole, S. V. Bhoraskar, and M. Bhadbhade, Appl. Phys. Lett. **80**, 4813 (2002).
[24] Q.Wu, N. Liu, Y. Zhang, W. Qian, X. Wanga and Z. Hua, J. Mater. Chem. C **3**, 1113-1117 (2015).
[25] E. Cappelli, D.M. Trucchi, S. Orlando, V. Valentini, A. Mezzi, S. Kaciulis, Appl. Phys. A **114**, 611–617 (2014).
[26] A. Mezzi, P. Soltani, S. Kaciulis, A. Bellucci, M. Girolami, M. Mastellone, D. M. Trucchi, Surf. Interface Anal. **50**, 1138–1144 (2018).
[27] M. Kuball, Surf. Interface Anal. **31**, 987–999 (2001).
[28] V. Lughi and D. R. ClarkeAppl. Phys. Lett. 89, 241911 (2006).
[29] P. Motamedi, K. Cadien, App. Surf. Sci. **315**, 104–109 (2014).
[30] V. M. Bermudez, T. M. Jung, K. Doverspike, and A. E. Wickenden, J. Appl. Phys. **79**, 110 (1996).
[31] F. Jin, and A. Beaver, Appl. Phys. Lett. **110**, 213109 (2017)